2018-01-0735

Investigation of Interior Noise from Generic Side-View Mirror Using Incompressible and Compressible Solvers of DES and LES

Author, co-author (Do NOT enter this information. It will be pulled from participant tab in MyTechZone)
Affiliation (Do NOT enter this information. It will be pulled from participant tab in MyTechZone)

Abstract

Exterior turbulent flow is an important source of automobile cabin interior noise. The turbulent flow impacts the windows of the cabins to excite the structural vibration that emits the interior noise. Meanwhile, the exterior noise generated from the turbulent flow can also cause the window vibration and generate the interior noise. Side-view mirrors mounted upstream of the windows are one of the predominant body parts inducing the turbulent flow. In this paper, we investigate the interior noise caused by a generic side-view mirror. The interior noise propagates in a cuboid cavity with a rectangular glass window. The exterior flow and the exterior noise are computed using advanced CFD methods: compressible large eddy simulation, compressible detached eddy simulation (DES), incompressible DES, and incompressible DES coupled with an acoustic wave model. The last method is used to simulate the hydrodynamic and acoustic pressure separately. The pressure fluctuations of the flow and noise are imposed on the window in the computation of the interior noise, but the reversal effect of the window vibration feeding back on the flow is neglected in the flow simulation. The localized flow characteristics are discussed. The energetic surface pressure appears in the regions where the shear layer from the mirror side edge impinges on the window. The contributions of the hydrodynamic and acoustic pressure to the interior noise are quantified. The acoustic component is found to be more efficient in the interior noise generation and to play the dominant role at high frequencies.

1. Introduction

Interior noise is a concern in the automobile industry to create a comfortable environment for drivers and passengers who would be exposed to the noise for a long period [1]. However, the flow-induced interior noise has not been efficiently controlled [2].

Side-view mirrors are important contributors to the interior noise in the cabins of automobiles. The high-energy vortices induced by the mirrors can generate significant exterior noise and powerful hydrodynamic impingement [2]. The interior noise induced by the exterior flow and noise was measured for a production car in road tests [3]. They also analyzed the contributions of the exterior acoustic and hydrodynamic pressure to the interior noise using an empirical statistical energy analysis (SEA) model. It was found that the exterior acoustic pressure is important although it is much lower than the hydrodynamic pressure by 20dB to 40dB at frequencies ranging from 100Hz to 5000Hz. In the study by Vanherpe et al. [3], compressible flow simulation was conducted to analyze the wavenumber-frequency spectra of the exterior surface pressure fluctuations on a plate that arise due to the impingement of the wake induced by a production mirror. Two domains associated with the hydrodynamic and acoustic pressure are clearly discerned in the spectra. The interior noise for a production mirror mounted on a generic vehicle model was studied experimentally and numerically [5]. In their study, the exterior surface pressure is decomposed into the hydrodynamic and acoustic pressure based on the wavenumber-frequency spectra. They reported that the acoustic pressure dominates the interior noise generation. The wavenumber-frequency spectra were further explored for a production mirror assembled on a production car in simulations and experiments [6]. The exterior acoustic pressure is found as the dominant interior noise source at high frequencies on most part of the window, except for the region near the mirror, where the hydrodynamic pressure is more effective. In a recent study by Schell and Cotoni [7], the flow-induced interior noise in a production car is predicted.

Apart from the production mirrors, a generic side-view (GSV) mirror was proposed [8, 9]. They studied the surface pressure and exterior far-field noise in simulations and experiments. The surface pressure fluctuations on the plate, which are generated due to the impingement of the wake, are the predominant exterior noise source. The shear layer developing from the mirror side edge impacts the plate and then forms powerful fluctuating pressure zones. Furthermore, the generic side-view mirror was studied using the incompressible LES (I-LES) and the incompressible detached eddy simulation (I-DES) [10]. The far-field exterior noise is predicted using the Ffowcs Williams and Hawkings (FW-H) acoustic analogy. Their results on the surface pressure are consistent with the experimental findings [8, 9].

The present study aims to investigate the flow-induced interior noise produced by the GSV mirror. The basic mechanisms of the noise generation process will be explored. Another purpose is to study the performances of different computational fluid dynamics (CFD) and computational aeroacoustics (CAA) methods for the prediction of the interior noise. The CFD methods include compressible large eddy simulation (C-LES), compressible DES (C-DES) and incompressible DES (I-DES). The CAA method is a coupled approach of the I-DES and an acoustic wave model (AWM). For the I-DES, the effects of the mesh topologies between a trimmed mesh and a polyhedral mesh will be discussed. Furthermore, the contributions of the noise sources, the exterior hydrodynamic and acoustic pressure, will be addressed. The importance to involve the exterior compressibility in the interior noise prediction will be clarified.

The configuration is described in section 2. The numerical methodologies employed in the simulations of the flow, the exterior noise and the interior noise are presented in section 3. The numerical

parameters, the boundary conditions and the computational meshes are presented in section 4. The results are presented and discussed in section 5. The conclusions are drawn in section 6.

2. Configuration

The configuration is illustrated in Figure 1. The GSV mirror is assembled on a plate. The dimensions of the mirror and the plate are designed by following the settings of experiments [8, 9], while the leading-edge corners of the plate are rounded to comply with the radiation of spherical acoustic waves generated from the wake induced by the mirror. A cavity is placed under the plate. A window that is made of glass with a thickness of 0.004m is set on the interface between the plate and the cavity. The surface pressure fluctuations of the flow stimulate the window to vibrate. The vibration then produces the interior noise in the cavity.

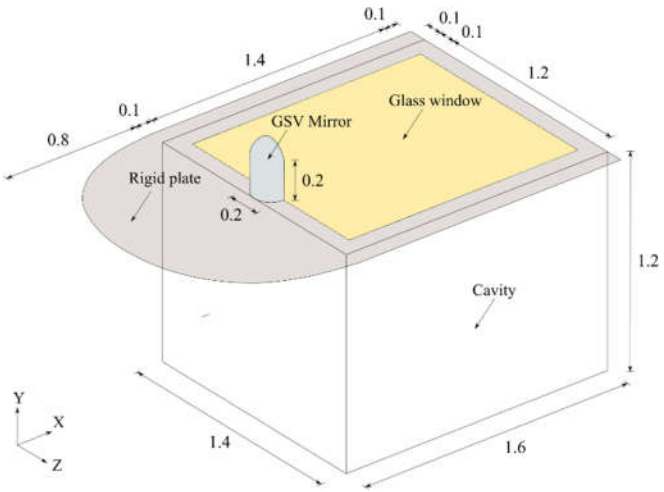

Figure 1. A sketch of the configuration that consists of the GSV mirror, the glass window and the cavity. The unit of length scales is m.

Both exterior and interior air are assumed as an ideal gas with the dynamic viscosity of $1.86 \times 10^{-5} Pa \cdot s$ and the molecular weight of $28.97\ kg/kmol$. The free-stream velocity vector of the exterior flow is $\vec{u}_\infty = (38.89, 0, 0) m/s$. The free-stream pressure is $p_\infty = 101.325\ kPa$. The free-stream temperature is $T_\infty = 300\ K$.

3. Numerical Methodology

3.1 Methods for Aeroacoustics

The governing equations of the continuity, momentum and energy that describe Newtonian flow are well known in the field of the fluid mechanics. Hence, they are not presented for the sake of brevity. As the simulation in present study is performed using the software STAR-CCM+, refer the details of the equations to the user guide of this software [11].

The flow is simulated with the methods such as the C-LES, the C-DES and the I-DES. Since the I-DES disregards the density change due to the compressibility, it cannot resolve acoustic waves in the computation. To simulate the noise for this method, an AWM is used.

3.1.1 Numerical Discretization of CFD Methods

The finite volume method is utilized to discretize the transport equations of continuity, momentum and energy. The segregated flow solver is used to solve the discretized equations. The Semi-Implicit Method for Pressure-Linked Equations (SIMPLE) algorithm is applied to the segregated flow solver. For the compressible flow solver, the density is obtained by means of solving the equation of state for the ideal gas after the pressure and temperature are updated.

The convection flux on a cell face is discretized by means of a hybrid second-order upwind and bounded-central scheme. The diffusion fluxes on the faces of both internal and boundary cells are discretized with a second-order scheme. The second-order hybrid Gauss-LSQ method is used in gradient computation, which involves the reconstruction of the field values on a cell face, the secondary gradients of the diffusion fluxes, the pressure gradients and the strain and rotation rates of a turbulence model.

A second-order implicit method is taken to discretize the time derivative. A dual time-stepping method with inner iterations at preconditioned pseudo-time steps is used in the time-marching procedure.

3.1.2 Turbulence Modelling

In the DES approach, the turbulence is simulated using the improved delayed detached eddy simulation (IDDES) [12]. The coefficients of the IDDES model adopts the default values in the software, i.e., $C_{DES,k-\omega} = 0.78$, $C_{DES,k-\varepsilon} = 0.61$, $C_{dt} = 20$, $C_l = 5$ and $C_t = 1.87$. The notations of the coefficients are referred to the user guide of STAR-CCM+ [11].

The compressibility correction is enabled for the k-ω model when the compressibility is involved in the simulation [13]. The turbulence dissipation is corrected with the addition of dilatation-induced dissipation as a function of the turbulent Mach number.

The method of all y^+ wall treatment that modifies the specific dissipation rate [14] is applied in near-wall cells. This method has an advantage of handling complex geometries. Since velocity over the complex walls vary in a wide range, it is difficult to ensure that the values of Δy^+ of all cells nearest the walls are either above a high value or below a small value. This problem is solved with the method of all y^+ wall treatment.

The turbulence modelling of the LES uses the Smagorinsky model [15]. The model coefficient determining the grid filter width for the subgrid scale (SGS) viscosity is set to $C_s = 0.1$. The model coefficient of the SGS turbulent kinetic energy is set to $C_{t,les} = 3.5$. The von Karman constant, κ, is 0.41. The near-wall treatment adopts the Van-Driest damping function [16] set with the coefficient $A_d = 25$.

3.1.3 Acoustic Wave Model for I-DES

The I-DES as an incompressible flow solver can only solve the hydrodynamic pressure without including the acoustic pressure. However, the acoustic pressure is an important contributor to the interior noise. An acoustic solver is therefore required to couple with the I-DES for the prediction of the interior noise.

The AWM developed based on the acoustic perturbation equations (APE) [17] is implemented in STAR-CCM+. The APE is derived by means of the linearization of the Navier-Stokes equations. It resolves the pressure and velocity perturbations produced by the acoustic waves. The acoustic propagation of the perturbations is described on the left-hand side of the equation system. The acoustic sources are formulated on the right-hand side. Due to the low Mach number in the present application, the convection of the mean flow is neglected in the propagation. The acoustic sources are formulated as pressure fluctuations [17]. The APE is reduced to the AWM as:

$$\frac{1}{c^2}\frac{\partial^2 p^a}{\partial t^2} - \nabla^2 p^a = -\frac{1}{c^2}\frac{\partial^2}{\partial t^2}P', \quad (1)$$

where p^a denotes the acoustic pressure, P' represents the hydrodynamic pressure fluctuations, c is the speed of sound and t is time. In the coupling method, the pressure fluctuations obtained from the I-DES are input to the AWM.

3.2 Methods for Structural Vibration and Interior Noise

The glass window and the cavity constitute a structure-acoustics system. The governing equations of the structure-acoustics system in frequency domain are given as [18]:

$$\begin{bmatrix} \boldsymbol{K}_S + i\omega\boldsymbol{D}_S - \omega^2\boldsymbol{M}_S & \boldsymbol{C}_{SA} \\ \omega^2\boldsymbol{C}_{SA}^T & \boldsymbol{K}_A + i\omega\boldsymbol{D}_A - \omega^2\boldsymbol{M}_A \end{bmatrix} \begin{pmatrix} \hat{\boldsymbol{u}}_S \\ \hat{\boldsymbol{p}}'_{in} \end{pmatrix} = \begin{pmatrix} \hat{\boldsymbol{p}}'_{ex} \\ 0 \end{pmatrix}, \quad (2)$$

where subscripts S and A represent the quantities associated with the window structure and the air. The exterior surface pressure fluctuations including the hydrodynamic and acoustic parts, $\hat{p}'_{ex}$, come from the CFD methods or the coupled CFD/AWM method. It is exerted on the glass window as a forcing boundary condition. The damping matrices of the window and air are denoted by $\boldsymbol{D}_S$ and $\boldsymbol{D}_A$. The structural/acoustic coupling matrix is denoted by $\boldsymbol{C}_{SA}$. The transpose of $\boldsymbol{C}_{SA}$ is $\boldsymbol{C}_{SA}^T$. Refer the detailed description of the vectors and matrices to the study by Coyette and Manera [18].

The structure-acoustics equations are solved using a finite element method implemented in Actran produced by Free Field Technologies [19].

4. Numerical Settings

4.1 Boundary Conditions and Solver Parameters

The computational domain and its dimensions are shown in Figure 2. The domain is constructed with round boundaries in the far field to reduce the incidence angles of acoustic waves propagating onto these boundaries. The upstream part of the domain has a spherical shape to comply with the shape of the plate. The distance between the mirror and the outlet is large enough to reduce artificial noise emitted from the vortices at the outlet.

The non-slip wall boundary condition is specified on the surfaces of the mirror and the plate. At the remaining of the domain boundaries, the free-stream boundary condition [20] is applied.

The under-relaxation factors for the velocity and the pressure in the segregated flow solver is set to 0.6 and 0.3. The under-relaxation factor for the turbulence transport equations is specified to 0.6.

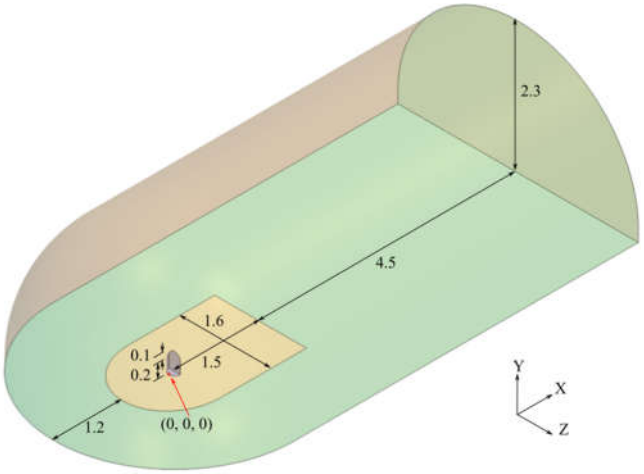

Figure 2. A schematic diagram of the computational domain, which is labeled with length scales. The unit is m.

The time step is set to $\Delta t = 1 \times 10^{-5}\ s$ to achieve the numerical stability in terms of the Courant number. The maximum number of inner iterations at every time step is 20. This number is sufficient to converge the solution according to the preliminary numerical tests performed for the configurations.

The window is modeled as a two-dimensional surface. The boundary between the window and cavity is set with zero displacements and rotations. A specular wall condition without absorption of reflected acoustic waves is imposed on the cavity walls.

4.2 Computational Meshes

An unstructured mesh generated using the trimmed mesh method is used in the flow simulations of the LES, C-DES and I-DES. In addition, an unstructured mesh is produced with the polyhedral mesh method and utilized in the coupled flow-aeroacoustics simulation of the I-DES and AWM.

The resolutions of the two meshes are controlled with the same parameters although the generation methods of the meshes are different. The size of the surface cells ranges between $0.001m$ and $0.01m$. The wall-normal heights of the near-wall cells are $1 \times 10^{-5}m$.

The volume cell sizes near the mirror edge are controlled below $0.001m$. The volume cells in the region where the flow wake exists are refined. This region starts from the mirror back surface and ends at $1.45m$ downstream of the mirror. The width of the region in the directions normal to the streamwise direction extends with a spread angle of 10^o. The largest cell size in the region is set to $0.005m$. The global maximum size of the volume cells is $0.05m$.

The mesh growth ratio ranges between 1.05 to 1.1 based on our previous studies [21-23]. The above mesh resolutions have been examined in preliminary simulations where meshes with coarser resolutions were employed.

The trimmed mesh in the cut-plane of $y = 0.1m$ is shown in Figure 3. The mesh is refined with 7 levels. The smallest cells, corresponding to the 7th refinement level, are located near the mirror edge. The region where the flow wake exists contains the cells refined at the 5th

refinement level. Most of the cells above the plate are refined above the 4th refinement level.

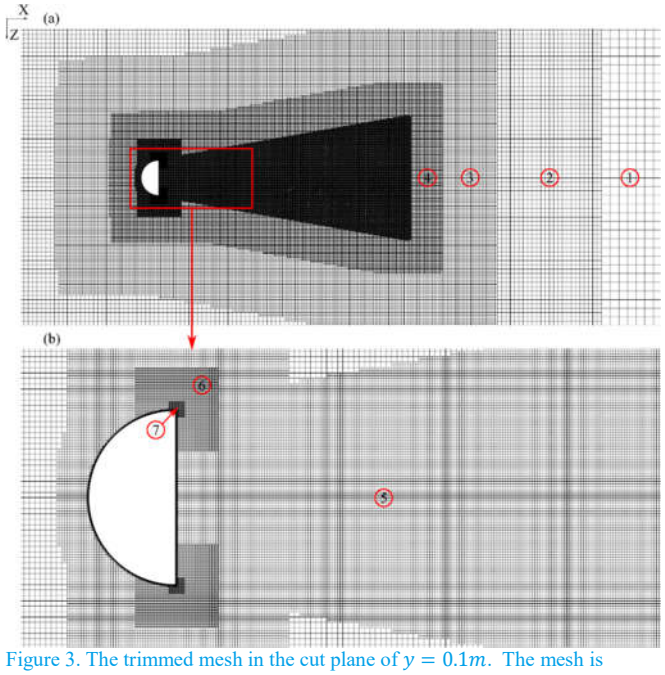

Figure 3. The trimmed mesh in the cut plane of $y = 0.1m$. The mesh is refined with 7 levels in addition to the prism elements in the boundary layers. The numbers marked in the red circles denote the local refinement level. The red rectangle in subfigure (a) marks the region that is magnified in subfigure (b).

The trimmed mesh in the cut-plane of $z = 0m$, which is the plane of the symmetry of the mirror geometry, is shown in Figure 4. The refined regions expand with the spread angle of 10^o in the direction along the y axis. The refinement enables a good mesh resolution for the flow structures in the shear layer and wake.

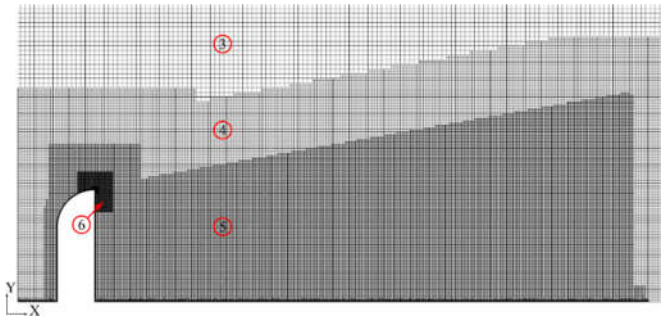

Figure 4. The trimmed mesh in the cut plane of $z = 0m$. The numbers in the red circles indicate the local refinement level. Note that the cells of the refinement level 7 are not clearly visualized due to their small sizes.

The polyhedral mesh is viewed in cut planes of $y = 0.1m$ and $z = 0m$ in Figure 5. The distribution of the refined regions in this mesh is consistent with the trimmed mesh. However, a smooth change of the cell sizes is observed in the polyhedral mesh. This is different from the trimmed mesh, where cells have a uniform size in a region at each refinement level.

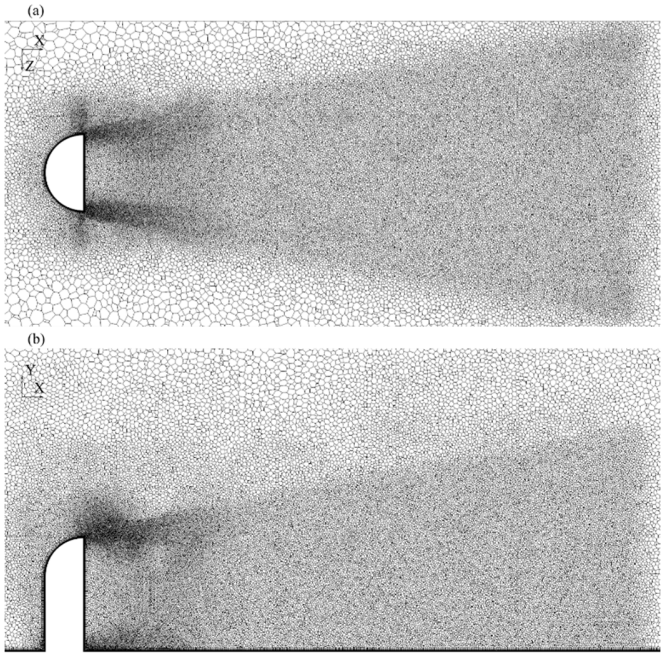

Figure 5. The polyhedral mesh in the cut planes of (a) $y = 0.1m$ and (b) $z = 0m$. The mesh is generated for the coupled I-DES/APE.

The trimmed mesh contains 21 million cells, 62 million faces and 21 million vertices. The polyhedral mesh has 8 million cells, 53 million faces and 42 million vertices.

A two-dimensional structured mesh is generated for the window, which is considered as a surface in the structure-acoustics system in the simulation. The cells have the same size of $0.0125m$. Another structured mesh is generated for the cavity. The cell size is $0.025m$. These meshes are shown in Figure 6.

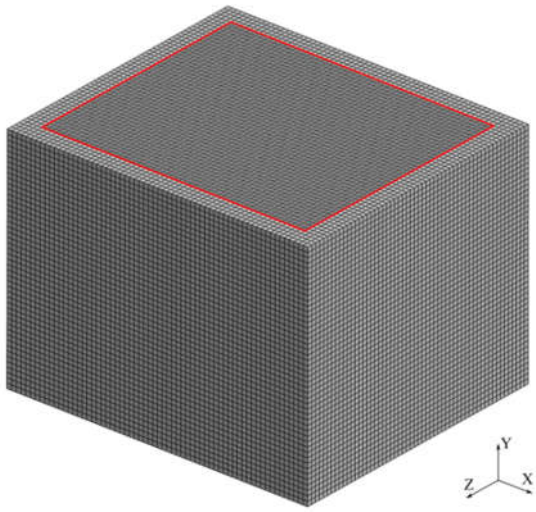

Figure 6. The structured meshes generated for the window and cavity. The window boundaries are marked with red lines.

5. Results and Discussion

The CFD simulations are performed with parallel computing on a cluster provided by the Swedish National Infrastructure for Computing. The hardware of the cluster is HP Cluster Platform 3000 with SL230s Gen8 nodes. Every node contains 2 sockets of 32 GB DDR3 1600 MHz memory. A socket has 8 cores of Intel Xeon Processor E5-2660 at 2.2 GHz.

The performances of the different CFD methods are evaluated by running the parallel computing of 48 cores. Comparison of the elapsed time per time step between the methods is displayed in Figure 7. The C-LES takes the shortest elapsed time. With the same mesh, the LES consumes less computational resources than the DES since it solves fewer equations. The elapsed time of the I-DES is slightly smaller than that of the C-DES. This suggests that the involvement of the compressibility in the simulations has limited influence to the computational speed. The I-DES with the polyhedral mesh takes much more computational resources as compared with the I-DES with the trimmed mesh. The reason is that the former mesh contains much more vertices than the latter mesh although the two meshes are generated with the same mesh density settings. When the AWM is used for reconstructing the exterior acoustic waves, the elapsed time increases by 1.2 times as compared with the I-DES without the AWM. The reason is that the acoustics simulation with the AWM needs additional computational resources.

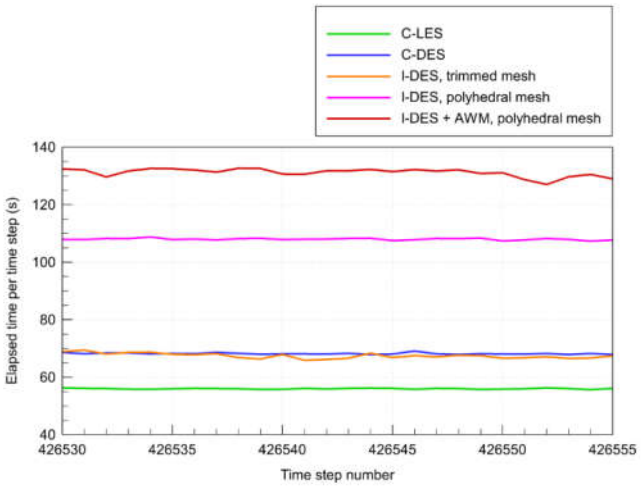

Figure 7. The elapsed time per time step consumed by the different CFD methods.

The instantaneous contours of Δy^+ of the near-wall cells are illustrated in Figure 8. All CFD methods with different meshes achieve the values of Δy^+ less than 1 in the most part of the surfaces, except for a narrow region along the plate edge. The large values are caused by high velocity gradients since the boundary condition at the plate edge is changed from the freestream boundary condition to the wall boundary condition. The small Δy^+ suggests that the boundary layers are well resolved in the simulations. The results from the C-DES and I-DES are consistent, but a wider wake region is observed in the C-LES. In addition, the contours upstream of the mirror and near the shear layers resolved with the C-LES are more fluctuating as compared with the DES methods.

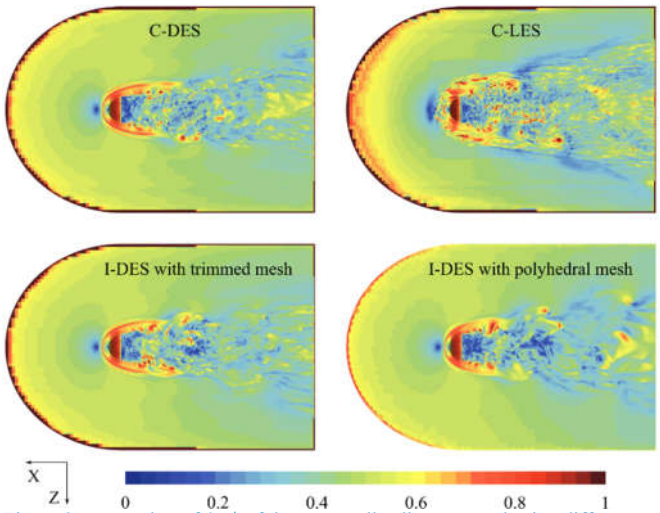

Figure 8. A snapshot of Δy^+ of the near-wall cells computed using different CFD methods.

To identify the vortices induced by the mirrors, instantaneous isosurfaces of the Q-criterion at $1.5 \times 10^6\ s^{-2}$ that are solved with the C-DES, are shown in Figure 9. Many vortices are observed in the wake. The horseshoe vortex is seen to initiate upstream of the mirror. The plate is subject to the impingement of the vortices. As the flow structures obtained from the other CFD methods and mesh are similar as the C-DES, they are not presented.

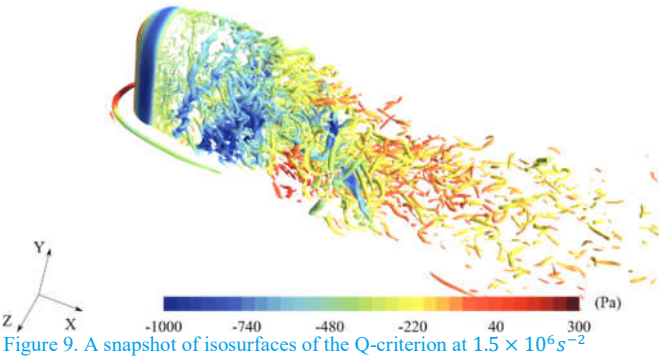

Figure 9. A snapshot of isosurfaces of the Q-criterion at $1.5 \times 10^6 s^{-2}$ simulated using the C-DES, colored with the instantaneous pressure $p - p_\infty$.

Hereafter, the statistical characteristics of the flow quantities are computed with the simulation duration of 0.2s, which corresponds to 39 times the flow characteristic time calculated in terms of the freestream velocity and mirror diameter. The time-averaged pressure coefficient is defined as $\langle C_p \rangle = (p - p_\infty)/(0.5\rho_\infty u_\infty^2)$, where the angle bracket denotes the time-averaged operator. The coefficient is computed at the monitors that are placed on the mirror surfaces. The specification of the monitors follows the experiments by Höld et al. [8] and Siegert et al. [9]. For the sake of brevity, four monitors are selected and discussed in this paper though we have computed the coefficients at all monitors. The positions of the selected monitors are illustrated in Figure 10. The selected monitors are called M5, M15, M25 and M34. The first three monitors are located on the front face of the mirror, and the last monitor on the back face. The coordinates of the monitor positions are given in Table 1.

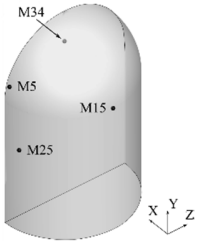

Figure 10. Illustration of the monitors on the mirror. The monitors are numbered by following the order in the experiments [8, 9]. The monitor, M34, is located on the back surface of the mirror.

Table 1. The coordinates of the selected monitors.

	$(x, y, z)m$
M5	$(0.094, 0.226, -0.096)$
M15	$(0, 0.2, 0)$
M25	$(0.074, 0.133, -0.097)$
M34	$(0.1, 0.25, 0)$

The values of $\langle C_p \rangle$ that are given by the different CFD methods and reported in the literature [8-10] are compared in Table 2. The DES methods and the I-LES [10] give larger coefficients at M5 near the mirror edge compared with the experimental data, while the C-LES provides a smaller coefficient. As indicated in Figure 8, the lower value is related to the phenomenon that the LES renders more fluctuations near the wall than the DES. The numerical and experimental results at M15, which is the stagnation point, are consistent. At M25, all numerical methods underestimate the coefficient as compared with the experiment. This monitor position is close to the smallest shear stress tensor magnitudes [10]. The present I-DES method with the trimmed or polyhedral meshes overestimates the coefficient at M34. This effect is associated with the compressibility (as compared with the C-DES) and the fluctuations resolved in the boundary layer (as compared with the C-LES).

Table 2. Time-averaged pressure coefficients $\langle C_p \rangle$ at the selected monitors.

	M5	**M15**	**M25**	**M34**
Siegert's experiments [9]	-0.629	0.886	-0.753	-0.484
Ask's I-DES [10]	-0.668	0.886	-1.112	-0.451
Ask's I-LES [10]	-0.727	0.898	-1.102	-0.443
I-DES 1 (trimmed mesh)	-0.65	0.896	-1.087	-0.407
I-DES 2 (polyhedral mesh)	-0.648	0.892	-1.081	-0.387
C-DES	-0.67	0.888	-1.078	-0.426
C-LES	-0.537	0.892	-0.925	-0.512

The root mean square (rms) values of the pressure fluctuations, which are defined as $p' - \langle p \rangle$, are displayed on the window in Figure 11. The contours from the DES methods are similar. This suggest that the influences from the compressibility and the cell topologies are not apparent. However, the wake region solved with the C-LES is wider in the spanwise direction than the DES methods. This behavior agrees with the phenomenon shown by Δy^+ in Figure 8. Therefore, the C-LES resolves more pressure fluctuations in the boundary layer.

The contours are asymmetric due to the limited simulation duration (0.2s) considered in computation of the rms values.

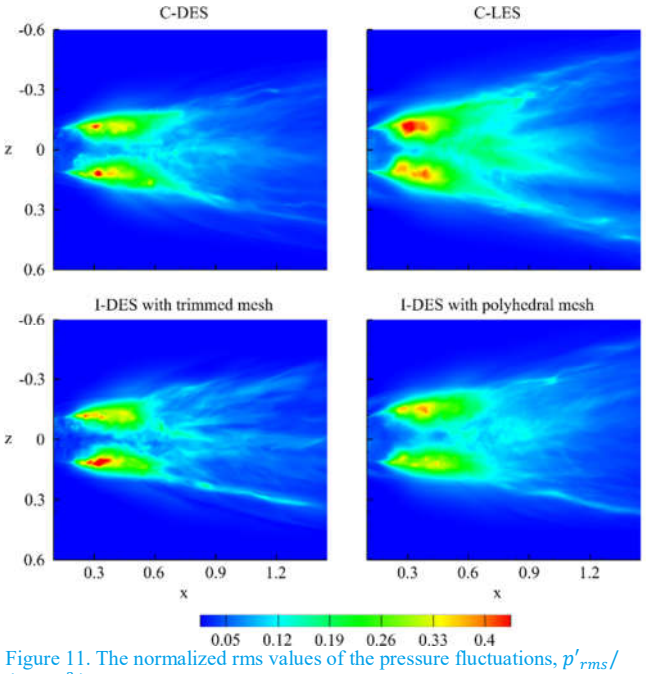

Figure 11. The normalized rms values of the pressure fluctuations, $p'_{rms}/(0.5\rho u_\infty^2)$, on the window, computed with the different CFD methods.

The pressure of the interior noise is collected at the microphones that are located at the corners and center of the cavity. The microphone positions are illustrated in Figure 12. There are 9 microphones in the cavity. The microphone, Mic. 1, is set at the center. The rest of the microphones are distributed at the corners. For the sake of brevity, Mics. 1 and 4 are chosen in the subsequent analysis.

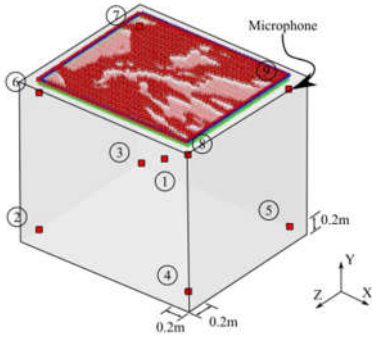

Figure 12. The microphone positions inside the cavity, where the microphone numbers are marked by the circles. The window is colored in red. The distances between the corners microphones to the cavity walls are labeled.

The spectra of the interior noise of the sound pressure levels (SPL), which are predicted based on the surface pressure fluctuations from the different CFD methods and meshes, are displayed in Figure 13. Given that 6 elements are needed to well resolve a wave, the maximum frequency that can be resolved by the current cavity mesh is 2267Hz. This indicates that the results above the maximum frequency are inaccurate. The upper limit of the frequency range in the figure is therefore set to 3000 Hz. All CFD method give comparable magnitudes at low frequencies below $1000Hz$, while above this frequency the compressible flow solvers (the C-LES and C-DES) give larger magnitudes than the I-DES. The large

magnitudes at the high frequencies are attributed to the compressibility. In the I-DES, the acoustic pressure is not solved so that the interior noise caused by the acoustic pressure is not included in the prediction. In addition, the interior noise caused by the exterior hydrodynamic pressure, which is obtained with the I-DES, is consistent between the trimmed and polyhedral meshes. The reason is that the cell topology has a limited effect in the simulation of the hydrodynamic pressure once the mesh resolution is refined enough to resolve flow structures.

In addition, the magnitudes predicted with the C-LES are larger than the C-DES at the high frequencies, as shown in Figure 13. According to Figures 8 and 11, the C-LES resolves more small-scale fluctuations in the boundary layer and the impinging vortices. The fluctuations form the noise sources at the high frequencies.

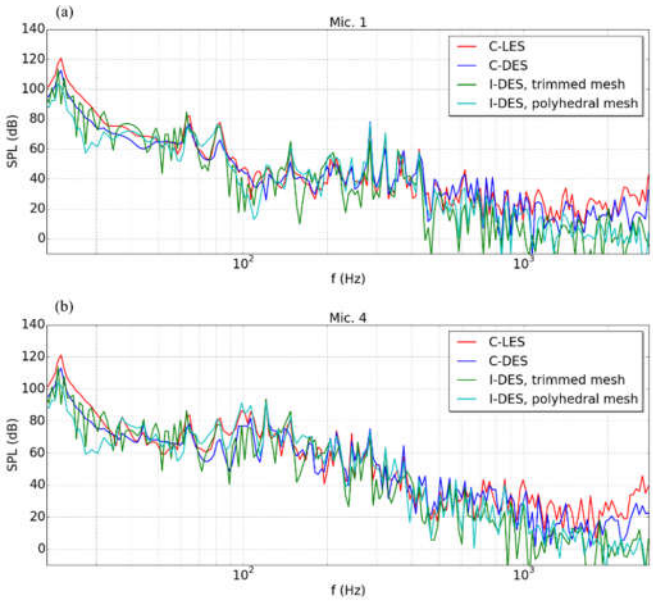

Figure 13. The spectra of the interior noise at the microphones (a) Mic. 1 and (b) Mic. 4, computed using the different CFD methods.

The spectra of the interior noise, which is computed based on the solutions of the coupled I-DES and AWM with the polyhedral mesh, are plotted in Figure 14. The interior noise is decomposed into two parts: a part produced by the exterior hydrodynamic pressure fluctuations, and the other part by the exterior acoustic pressure fluctuations. The hydrodynamic part is predicted by employing the I-DES solution, which includes only the exterior hydrodynamic pressure. The prediction of the acoustic part is conducted based on the AWM solution. It is observed that the magnitudes of hydrodynamic part are larger than those of the acoustic part at low frequencies. The acoustic part exceeds the hydrodynamic part for the frequencies above $1000Hz$. This observation suggests that the exterior acoustic pressure is predominant in the generation of the interior noise at high frequencies.

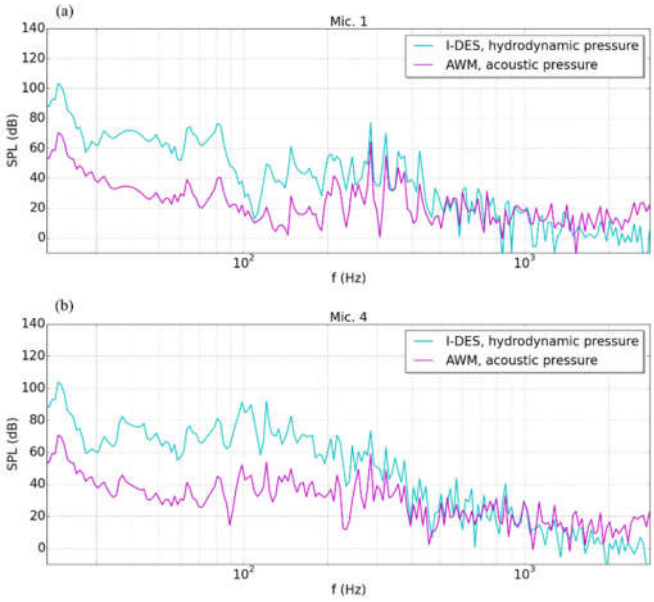

Figure 14. The spectra of the hydrodynamic and acoustic part of the interior noise at the microphones (a) Mic. 1 and (b) Mic. 4. The noise parts are computed based on the exterior hydrodynamic pressure fluctuations from the I-DES and the exterior acoustic pressure fluctuations from the AWM, respectively.

The compressible flow solvers (C-LES and C-DES) are used to obtain the compressible pressure including both hydrodynamic and acoustic pressure, whereas the incompressible flow solver (I-DES) gives only the hydrodynamic pressure. Therefore, the compressible flow solvers enable the prediction of the total interior noise. The incompressible flow solver gives the hydrodynamic interior noise.

As displayed in Figure 13, the total interior noise does not have a dropping trend above 1000Hz, in contrast to the hydrodynamic interior noise. By applying the AWM to reconstruct the acoustic pressure based on the incompressible flow solution, it is found that this non-dropping trend is due to the acoustic interior noise, which is dominant and does not drop at high frequencies, as shown in Figure 14. Although the different CFD and CAA methods are utilized to simulate the flow and noise, they predict similar trends for the total interior noise. This phenomenon is different from experimental results reported by Hartmann et al. [5], where a dropping trend was observed. In their experiments, a real mirror assembled onto a generic vehicle model with a cabin was investigated. By means of creating exterior acoustic excitation with a loudspeaker, they also demonstrated that the acoustic pressure plays an important role in the interior noise generation. Moreover, an enlarged mirror was found producing larger interior noise, even though the exterior pressure induced by this mirror has nearly the same magnitudes as the baseline mirror above 250Hz. The effect of the same magnitudes is caused by the hydrodynamic pressure, since the exterior pressure is dominated by the hydrodynamic pressure. Based on this effect, they concluded that the acoustic pressure is the major cause to make the interior noise change significantly. Comparison of the enlarged mirror and baseline mirror reveals another fact, namely that the acoustic exterior pressure magnitudes are sensitively dependent on the mirror geometry and dimensions. It is therefore understandable that the generic mirror in the present study produces different interior noise spectra above 1000Hz, as compared to the real mirror by Hartmann et al. [5]. Nonetheless, interesting future works would be to perform a cross comparison between the generic mirror and Hartmann's real mirror based on the same numerical and experimental methodologies, and to

explore the influence of mirror geometries on the interior noise generation.

The hydrodynamic interior noise is comparable to the total interior noise between 100Hz and 1000Hz, as shown in Figure 13. This phenomenon is explainable based on the results observed in Figure 14. Below 400Hz, the hydrodynamic interior noise is approximately 20--40dB larger than the acoustic interior noise. The acoustic interior noise is therefore negligible compared with the total interior noise, which is the sum of the hydrodynamic and acoustic noise. In the frequency range of 400 to 1000Hz, Figure 13 shows that the hydrodynamic noise magnitudes are slightly lower than the total noise magnitudes. Since the log scale is used in the SPL definition, the addition of the acoustic noise, which has similar magnitudes to the hydrodynamic noise between 400 and 1000Hz (see Figure 14), cannot lead to significant magnitude increases in the total noise.

6. Conclusions

In this paper, we numerically investigate the interior noise in a cuboid cavity. The interior noise is generated by the window vibration that is excited by the exterior flow and the flow-induced noise of a generic side-view mirror. The exterior flow and noise are simulated using the advanced CFD and CAA methods such as C-LES, C-DES, I-DES, and I-DES coupled with the AWM. The coupled method simulates the exterior hydrodynamic and acoustic pressure separately.

The C-LES resolves more pressure fluctuations in the boundary layer than the DES methods. A consequence is that the interior noise predicted with the C-LES is larger than the C-DES at the high frequencies. It is found that the spanwise width of the wake region obtained with the C-LES is wider than for the DES methods. By comparing the results of the I-DES between the trimmed and polyhedral meshes, the cell topology is found with a limited influence on the solution of the hydrodynamic pressure given that the mesh resolution is sufficiently refined.

The exterior hydrodynamic pressure contributes to the major part of the interior noise in the low frequency range, whereas the exterior acoustic pressure plays the dominant role above $1000Hz$. The compressibility should thus be considered in the CFD simulation for the further prediction of the interior noise. However, the incompressible solver can also be valid if an acoustic solver is coupled with it to resume the simulation of acoustic waves.

References

1. Zwicker, E., and Fastl, H., “Psychoacoustics, Facts and Models,” (Springer, 1990), 265-269.
2. Buchheim, R., Dobrzynski, W., Mankau, H., and Schwabe, D., “Vehicle Interior Noise Related to External Aerodynamics,” Int. J. Vehicle Design 3(4):398-410, 1982.
3. Dejong, R. G., Bharj, T. S., and Lee, J. J., “Vehicle Wind Noise Analysis Using a SEA Model with Measured Source Levels,” SAE Technical Paper:2001-01-1629, 2001.
4. Vanherpe, F., Baresh, D., Lafon, P., and Bordji, M., “Wavenumber-Frequency Analysis of the Wall Pressure Fluctuations in the Wake of a Car Side Mirror,” AIAA Paper 2011-2936, 2011.
5. Hartmann, M., Ocker J., Lemke T., et al., “Wind Noise Caused by the A-pillar and the Side Mirror Flow of a Generic Vehicle Model,” AIAA paper 2012-2205, 2012.
6. Okutsu, Y., Hamamoto, N., and Yanagimoto, K., Doi, K., and Nakamura, Y., “The Character of the Turbulent Wall Pressure Spectrum at Subconvective Wavenumbers and a Suggested Comprehensive Model,” J. Environ. Eng. 8:41-56, 2013.
7. Schell, A., and Cotoni, V., “Flow Induced Interior Noise Prediction of a Passenger Car,” SAE Int. J. Passeng. Cars – Mech. Syst. 9(3):1053-1062, 2016.
8. Höld, R., Brenneis, A., Eberle, A., Schwarz, V., and Siegert, R., “Numerical simulation of Aeroacoustic Sound Generated by Generic Bodies Placed on a Plate. Part 1. Prediction of Aeroacoustic Sources,” AIAA Paper 99-1896, 1999.
9. Siegert, R., Schwarz, V., and Reichenberger, J., “Numerical Simulation of Aeroacoustic Sound Generated by Generic Bodies Placed on a Plate. Part 2. Prediction of Radiated Sound Pressure,” AIAA Paper 99-1895, 1999.
10. Ask, J., and Davidson, L., “The Sub-Critical Flow Past a Generic Side Mirror and Its Impact on Sound Generation and Propagation,” AIAA Paper 2006-2558, 2006.
11. STAR-CCM+ User Guide (Version 12.04), Siemens PLM Software, 2017.
12. Shur, M.L., Spalart, P.R., Strelets, M.Kh., and Travin, A.K., “A Hybrid RANS-LES Approach with Delayed-DES and Wall-Modelled LES Capabilities,” International J. Heat and Fluid Flow, 29(6):1638-1649, 2008.
13. Sarkar, S., Erlebacher, G., Hussaini, M. Y., and Kreiss, H. O., “The Analysis and Modelling of Dilatational Terms in Compressible Turbulence,” J. Fluid Mech. 227:473-493, 1991.
14. Wilcox, D.C., “Turbulence Modeling for CFD, 2n Edition,” (DCW Industries Inc., 1998).
15. Smagorinsky, J., “General Circulation Experiments with the Primitive Equations: Part I, The Basic Experiment,” Monthly Weather Review 91:99-164, 1963.
16. van Driest, E. R., “On Turbulent Flow Near a Wall,” J. Aero. Sci. 23:1007-1011, 1956.
17. Ewert, R., and Schroder, W., “Acoustic Perturbation Equations Based on Flow Decomposition via Source Filtering,” J. Comput. Phys., 188:365-398, 2003.
18. Coyette, J.-P., and Manera, J., “Application of Acoustic FEA to the Automotive and Aircraft Industry,” SAE Technical Paper:2010-36-0519, 2010.
19. Free Field Technologies (FFT), “Actran 16.0 Users Guide Volume 1 Installation, Operations, Theory and Utilities,” 2016.
20. Colonius T., Lele S. K., and Moin, P., “Boundary Conditions for Direct Computation of Aerodynamic Sound Generation. AIAA J. 31:1574-1582, 1993.
21. Yao, H.-D., Davidson, L., and Eriksson, L.-E., et al., “Surface Integral Analogy Approaches to Computing Noise Generated by a 3D High-Lift Wing Configuration,” AIAA paper, 2012-0386.
22. Yao, H.-D., Davidson, L., and Eriksson, L.-E., et al., “Surface Integral Analogy Approaches for Predicting Noise from 3D High-Lift Low-Noise Wings,” Acta Mech. Sin. 30(3):326-338, 2014.
23. Yao, H.-D., Davidson, L., and Eriksson, L.-E., “Noise Radiated by Low-Reynolds Number Flows past a Hemisphere at Ma=0.3,” Phys. Fluids 29(7):076102, 2017.

Contact Information

Mailing address: Department of Mechanics and Maritime Sciences, Chalmers University of Technology, Horsalsvagen 7A, Gothenburg, Sweden, SE-41296

Email address: huadong.yao@chalmers.se

Telephone number: +46 31 772 1405

Acknowledgments

This work has been supported by Fordonsstrategisk Forskning och Innovation (FFI) of VINNOVA-Sweden's innovation agency (grant no. 2014-01386). The authors offer their appreciation to the Swedish National Infrastructure for Computing (SNIC), who provided computer resources.

Definitions/Abbreviations

C-LES	compressible large eddy simulation
I-LES	incompressible LES
C-DES	compressible DES
I-DES	incompressible DES
RANS	the Reynolds-averaged Navier–Stokes equations
CAA	computational aeroacoustics
APE	acoustic perturbation equations
AWM	acoustic wave model
GSV mirror	generic side-view mirror